

A₂TiO₅ (A = Dy, Gd, Er, Yb) at High Pressure

Sulgiye Park,^{*},^{†,ID} Dylan R. Rittman,[†] Cameron L. Tracy,[†] Karena W. Chapman,^{‡,ID} Fuxiang Zhang,[§] Changyong Park,^{||,ID} Sergey N. Tkachev,[†] Eric O’Quinn,[#] Jacob Shamblin,^{#,ID} Maik Lang,[#] Wendy L. Mao,^{†,V} and Rodney C. Ewing[†]

[†]Department of Geological Science, Stanford University, Stanford, California 94305, United States

[‡]X-ray Science Division, Advanced Photon Source, Argonne National Laboratory, Argonne, Illinois 60439, United States

[§]Materials Science and Technology Division, Oak Ridge National Laboratory, Oak Ridge, Tennessee 37831, United States

^{||}HPCAT, Carnegie Institution of Washington, Argonne, Illinois 60439, United States

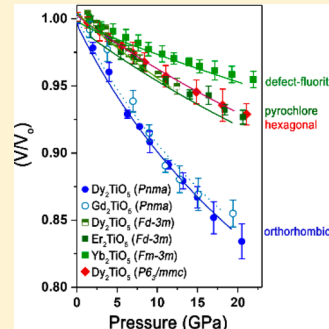
[†]Center for Advanced Radiation Sources, University of Chicago, Chicago, Illinois 60637, United States

[#]Department of Nuclear Engineering, University of Tennessee, Knoxville, Tennessee 37996, United States

^VStanford Institute for Materials & Energy Sciences, SLAC National Accelerator Laboratory, Menlo Park, California 94025, United States

Supporting Information

ABSTRACT: The structural evolution of lanthanide A₂TiO₅ (A = Dy, Gd, Yb, Er) at high pressure is investigated using synchrotron X-ray diffraction. The effects of A-site cation size and of the initial structure are systematically examined by varying the composition of the isostructural lanthanide titanates and the structure of dysprosium titanate polymorphs (orthorhombic, hexagonal, and cubic), respectively. All samples undergo irreversible high-pressure phase transformations, but with different onset pressures depending on the initial structure. While each individual phase exhibits different phase transformation histories, all samples commonly experience a sluggish transformation to a defect cotunnite-like (*Pnma*) phase for a certain pressure range. Orthorhombic Dy₂TiO₅ and Gd₂TiO₅ form *P2₁am* at pressures below 9 GPa and *Pnma* above 13 GPa. Pyrochlore-type Dy₂TiO₅ and Er₂TiO₅ as well as defect-fluorite-type Yb₂TiO₅ form *Pnma* at ~21 GPa, followed by *I*₁*m*₃*m*. Hexagonal Dy₂TiO₅ forms *Pnma* directly, although a small amount of remnants of hexagonal Dy₂TiO₅ is observed even at the highest pressure (~55 GPa) reached, indicating kinetic limitations in the hexagonal Dy₂TiO₅ phase transformations at high pressure. Decompression of these materials leads to different metastable phases. Most interestingly, a high-pressure cubic X-type phase (*I*₁*m*₃*m*) is confirmed using high-resolution transmission electron microscopy on recovered pyrochlore-type Er₂TiO₅. The kinetic constraints on this metastable phase yield a mixture of both the X-type phase and amorphous domains upon pressure release. This is the first observation of an X-type phase for an A₂BO₅ composition at high pressure.



INTRODUCTION

A₂TiO₅ compositions (A = lanthanides, Y) are of great interest because of their high dielectric constants, low susceptibility to radiation damage, high ion selectivity, thermal stability, and robust mechanical strength.^{1–4} These compounds find use as neutron absorbers in control rods,^{5,6} electrolytes in solid oxide fuel cells,^{7–9} charge-trapping flash memory devices,¹⁰ biosensors,¹ and gates for electrolyte–insulator–semiconductor devices.¹

Early studies reported a general phase diagram for the A₂TiO₅ series, which exhibits polymorphic phase transformations as a function of A-site cationic radius and temperature.^{11–13} On the basis of these studies, A₂TiO₅ under ambient conditions exists in either (1) an orthorhombic structure for materials with A-site cations equal to or larger than Ho (La–Ho), or (2) a cubic structure for materials with A-site cations equal to or smaller than Y (Dy–Lu, Sc, and Y) (Figure 1). For orthorhombic A₂TiO₅ (*Pnma*; *o*-A₂TiO₅), the A-site

cation is in 7-fold coordination, forming a monocapped octahedron, while Ti is coordinated to five oxygens, forming an off-center square pyramid.^{11–13} There are no mixed-occupancy sites, and the neighboring polyhedra share corners to form a chain along the *c* axis. The cubic A₂TiO₅ adopts either a pyrochlore-type phase (*Fd*₃*m*; *p*-A₂TiO₅), which is isostructural with rare-earth titanates of A₂Ti₂O₇ stoichiometry (with the exception of La₂Ti₂O₇), or a defect-fluorite phase (*Fm*₃*m*; *df*-A₂TiO₅). These two cubic structures are related and are derived from the AO₂ fluorite structure.^{14,15} However, the pyrochlore-type (*p*-type) structure has an ordering of vacant anion sites on the fluorite-like anion sublattice and of the two cations.^{14,15} The defect-fluorite structure has both A and B disordered over a single site with randomly arranged vacancies on the anion sublattice, maintaining charge balance. The long-

Received: December 13, 2017

Published: February 8, 2018



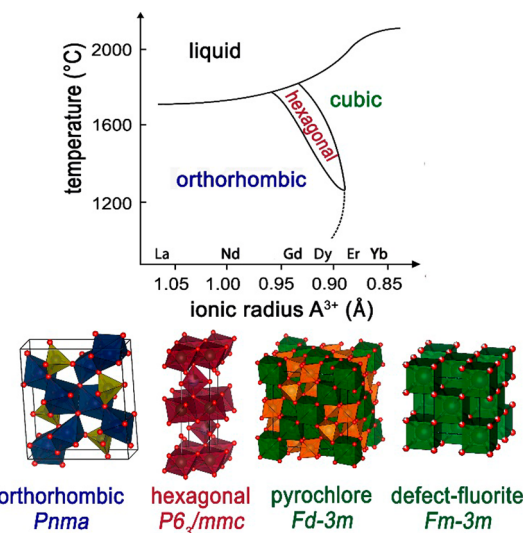


Figure 1. Temperature stability diagram for the series of compounds with $A_2\text{TiO}_5$ stoichiometry, adapted from Shepelev and Petrova.¹² The structures of orthorhombic, hexagonal, pyrochlore, and defect-fluorite $A_2\text{TiO}_5$ are shown for each (from left to right).

range isometric ordering in $A_2\text{TiO}_5$ mainly depends on the synthesis method (e.g., coprecipitation, shock-wave processing, solid-state reaction, and ball milling) and the A-site cation radius.¹⁶ Under the same synthesis conditions, smaller A-site cations (e.g., Yb) tend to yield a defect-fluorite structure. This is attributed to an enhanced disordering of the corner-shared tetrahedral networks from cation mixing that is facilitated by the low formation enthalpy of antisite defects associated with their size similarity to Ti. The different subgroup (ordered-pyrochlore versus disordered-fluorite) of this cubic phase can also be modified by varying the cooling rate, such that a slower cooling results in an ordered pyrochlore phase, while fast quenching from high temperature results in a fluorite structure due to kinetic limitations on ordering.^{16–19}

In addition to orthorhombic and cubic phases, a hexagonal polymorph ($P6_3/mmc$; $h\text{-}A_2\text{TiO}_5$) is formed for $A_2\text{TiO}_5$ materials at high temperature (>1350 °C, 1 atm), when the A-site is occupied by Eu–Ho. This hexagonal phase exhibits an ABABAB layered close-packed configuration with six layers, of which the first, second, fourth, and fifth layers are occupied by octahedrally coordinated lanthanides. The third and sixth layers are mixed sites, partially occupied by the lanthanide and Ti cations. As is the case for the cubic phases, a metastable hexagonal polymorph can be recovered via high-temperature processing by changing the cooling rate. Such synthesis has been reported for Dy_2TiO_5 , where a sol–gel technique was applied with various cooling rates.^{20,21}

Recently, Zhang et al. reported the quenched hexagonal phases of $o\text{-Nd}_2\text{TiO}_5$ and $o\text{-La}_2\text{TiO}_5$ following compression to above 10 GPa and subsequent decompression.²² The compounds undergo reconstructive phase transformations, and the quenchable hexagonal phase is isomorphous with the high-temperature polymorph of $h\text{-}A_2\text{TiO}_5$.²² The result demonstrated that, in addition to temperature, pressure can be used to “tune” the structure of materials in the $A_2\text{TiO}_5$ system. Despite the importance of $A_2\text{TiO}_5$ materials in engineering applications, there exists only one previous study that investigated the effects of high pressure on orthorhombic $A_2\text{TiO}_5$ compounds ($A = \text{La, Nd}$).²² Here we conduct a

systematic study of the high-pressure behavior of $A_2\text{TiO}_5$ ($A = \text{Dy, Gd, Er, Yb}$) compounds up to ~50 GPa. The family of $A_2\text{TiO}_5$ structure types has many applications, which makes the study of their basic behavior at high pressure useful. By varying the composition of the isostructural $A_2\text{TiO}_5$ and the structure of polymorphic $A_2\text{TiO}_5$, respectively, this investigation constrains the effects of both chemical composition and initial structure on the high-pressure phase behavior. Initial atomic ordering under ambient conditions is characterized using synchrotron-based X-ray total scattering and pair distribution function analysis (X-ray PDF). In situ high-pressure responses are determined by synchrotron X-ray diffraction (XRD) and Raman spectroscopy. The recovered high-pressure phase is additionally studied using transmission electron microscopy (TEM). All materials exhibit irreversible phase transformations. While the phase transition pressures are different, all of them undergo a defect cotunnite-like phase ($Pnma$) over a range of 30–40 GPa. Cubic $A_2\text{TiO}_5$ quenches in a metastable X-type phase ($Im\bar{3}m$), which is reported for the first time in $A_2\text{TiO}_5$ -type compositions.

EXPERIMENTAL SECTION

Polycrystalline Gd_2TiO_5 , Er_2TiO_5 , and Yb_2TiO_5 samples were synthesized from well-mixed Ln_2O_3 (99.9%) and TiO_2 (99.9%) powders by solid-state reactions at high temperature. The powders were compressed with a hand press (~15 MPa) without specific orientation, after which they were sintered at 1200 °C for 24 h. To further homogenize the reaction products, the pellets were reground and heated at 1450 °C multiple times for 48–72 h. The orthorhombic and hexagonal polymorphs of Dy_2TiO_5 were prepared by heating at 1300 and 1500 °C for 12 h, respectively. The cooling rates were kept at below 5 °C/min. The cubic Dy_2TiO_5 sample was prepared by pressing the powders into a 4 in. rod and melting in an image furnace using optical float zoning.

The synthesized samples were characterized using X-ray total scattering at beamline 11-ID-B of the Advanced Photon Source (APS), Argonne National Laboratory (ANL). Polycrystalline powder samples were packed into polyimide capillaries, which were sealed with epoxy. An X-ray energy of 90.5 keV ($\lambda = 0.137$ Å) was used. A large amorphous silicon-based area detector was used to record two-dimensional diffraction images, which were integrated using the software Fit2D²³ with a CeO_2 standard for calibration. The integrated data were then used to generate the PDFs, $G(r)$, using the software PDFgetX2,²⁴ after the polyimide capillary background was subtracted. Refinement of the PDF data was performed using PDFGUI, where a Q_{damp} (the Gaussian dampening envelope accounting for limited Q resolution) value of 0.04 and σ ratio (the reduction factor for PDF peak widths accounting for correlated motion of bound atoms) of 0.8 were applied for all patterns. The PDF displays the interatomic distance distribution (or probability of finding atomic pairs a distance r apart) on the basis of Fourier transform techniques, suitable for providing information on short-range local ordering.

High-pressure experiments were performed with symmetric diamond anvil cells (DACs), each with a pair of 300 μm culet diamonds. Rhodium and tungsten gaskets were indented to a thickness of ~25–30 μm, and a hole with a diameter of 100–120 μm was drilled in the center to serve as a sample chamber. For in situ high pressure measurements, fluid pressure media (ethanol methanol for Gd_2TiO_5 and silicone oil for all other samples) was used.²⁵ For transmission electron microscopy postanalysis, additional high-pressure experiments were conducted using Ne gas as a pressure medium to minimize the effects of residual silicone oil. Pressure in the DAC was determined using ruby fluorescence method up to ~50 GPa, and the pressure was increased at 2 GPa steps at room temperature.²⁶ The system was allowed to equilibrate for 5–10 min at each pressure point. The pressure before and after the XRD measurements varied by less than 1 GPa for all samples studied.

Pressure-induced structural changes were characterized with angle dispersive XRD at beamline 16-BM-D of the Advanced Photon Source (APS), Argonne National Laboratory (ANL). In contrast to PDF analysis, which probes short-range ordering, XRD provides information on long-range ordering and periodicity. Debye rings were recorded with a Mar345 image plate detector, and the images were integrated azimuthally using the software Dioptas.²⁷ Rietveld refinement was performed using the Fullprof suite.^{28,29} For all patterns, backgrounds were fit with a sixth-order polynomial and the diffraction peak profile was fitted with pseudo-Voigt functions. Atomic positions and unit cell parameters were then refined. For volume changes as a function of pressure, data were fit to an isothermal Birch–Murnaghan equation of state using EosFit7-GUI^{30,31} to determine the bulk modulus (B_0) of each sample. The order of the Birch–Murnaghan equation was chosen on the basis of the slope of normalized pressure versus strain, taking into consideration the error bars. Because there was almost no change in the normalized pressure as a function of strain ($B' = 4$), the second-order Birch–Murnaghan equation was used.^{32,33}

Samples from the DACs after decompression were further analyzed using transmission electron microscopy (TEM). Samples quenched from the highest pressure reached (~ 50 GPa) were dispersed on holey-carbon-coated copper TEM grids. Images were collected using an FEI Tecnai instrument operating at 200 kV in bright-field mode. The diffraction images were then analyzed using Gatan Digital Micrograph.

RESULTS AND DISCUSSION

Structures under Ambient Conditions. Figure 2 displays representative (a) X-ray atomic pair distribution function

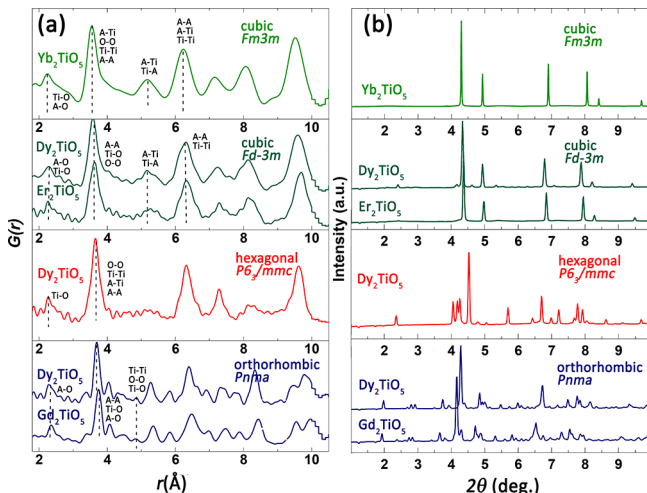


Figure 2. (a) X-ray PDF and (b) XRD of orthorhombic (blue), hexagonal (red), pyrochlore (light green), and defect-fluorite (dark green) A₂TiO₅ at ambient pressure and temperature. Both PDF and XRD data show well-crystalline A₂TiO₅ phases. The difference in the local bonding and ordering as shown in the PDFs is in agreement with the long-range structures. All measurements were collected with an X-ray energy of 90.5 keV ($\lambda = 0.137$ Å).

(PDF) analysis and (b) X-ray power diffraction (XRD) of A₂TiO₅ compounds under ambient conditions, grouped into three different structure types: orthorhombic (Dy₂TiO₅), hexagonal (Dy₂TiO₅), and cubic (Dy₂TiO₅, Yb₂TiO₅, and Er₂TiO₅). Patterns of the initial samples are highly crystalline A₂TiO₅ phases with no unreacted products or other impurity phases. Lattice parameters from the refined XRD patterns are reported in Table 1 and are in good agreement with previous investigations.^{2,12,13,34,35,21,20,36}

Table 1. Chemical Composition, Space Group, and Lattice Parameters Refined from XRD Patterns for All Compositions under Ambient Conditions

	<i>a</i> (Å)	<i>b</i> (Å)	<i>c</i> (Å)	α, β, γ (deg)	volume, <i>V</i> ₀ (Å ³)
Yb ₂ TiO ₅ (<i>Fm</i> $\bar{3}m$)	5.08(3)	5.08(3)	5.08(3)	90	131.34(3)
Er ₂ TiO ₅ (<i>Fd</i> $\bar{3}m$)	10.14(4)	10.14(4)	10.14(4)	90	1043.92(6)
Dy ₂ TiO ₅ (<i>Fd</i> $\bar{3}m$)	10.35(3)	10.35(3)	10.35(3)	90	1108.63(10)
Dy ₂ TiO ₅ (<i>P</i> 6 ₃ / <i>mmc</i>)	3.63(2)	3.63(2)	11.92(1)	90, 120	157.20(2)
Dy ₂ TiO ₅ (<i>Pnma</i>)	10.38(1)	11.21(2)	3.71(3)	90	431.66(2)
Gd ₂ TiO ₅ (<i>Pnma</i>)	10.27(6)	11.11(1)	3.68(2)	90	420.21(2)

In orthorhombic A₂TiO₅ compounds, the A–O, A–A, and Ti–O bond distances increase with increasing A-site cation radius, evidenced by increases in PDF peak positions to higher r (Å) with lanthanide cation substitution (Figure 2a). The increase in the bond distances is attributed to the increased cationic size. The bond distance change is less pronounced in cubic A₂TiO₅ compounds, most likely due to the symmetrical constraints of the ordered-pyrochlore phase. Concurrent with the increase in the bond distance of orthorhombic structures, the amount of disorder decreases, denoted by the subtle decrease in the full width at half-maximum of the corresponding peaks. This is attributed to the increased cation size mismatch, which is often accompanied by more strict topological constraints (or less structural freedom) and increased energetics of disordering. This trend is consistent with the previous literature, which reported a decrease in disorder with an increase in the A-site cation radius.^{37–39}

Among the three phases, o-A₂TiO₅ exhibits the most complex local structure, consistent with its lower symmetry. The local structure of the h-Dy₂TiO₅ resembles that of the cubic phase more so than the orthorhombic phase, but it lacks an A–Ti bond pair that appears at $r(\text{\AA}) \approx 5.3$ Å (Figure 2a). The absence of this peak in the h-Dy₂TiO₅ phase is attributed to a partial cation disordering. In the long-range periodicity, the difference in the *p*-type and *df*-type of the A₂TiO₅ phases is evidenced by the less intense supercell XRD diffraction maxima indicative of the pyrochlore structure, such as those at $2\theta = 4.8, 12.1, 14.5^\circ$ which are due to the (111), (133), and (155) spacings, respectively (Figure 2b). The ordered-pyrochlore unit cell also has a cell parameter, *a*, that is twice that of the fluorite structure. The more intense diffraction maxima at $2\theta = 9.7$ (222), 11.2 (004), 15.8 (044), 18.6° (226) are from fluorite-substructure ordering.

A₂TiO₅ at High Pressures. Selected XRD patterns of A₂TiO₅ at various pressures are shown in Figure 3. All samples exhibit three general changes with increasing pressure: broadening of the diffraction maxima, disappearance and appearance of peaks, and the growth of broad diffuse scattering bands. Broadening of peaks can be attributed to the microstrain caused by compression of particles in the system, which distorts the atomic spacings near the contact points. Concurrent with peak broadening is the disappearance of diffraction maxima and the appearance of new maxima, indicating pressure-induced phase transformations. For all samples, the phase transformation is followed by partial amorphization, illustrated by

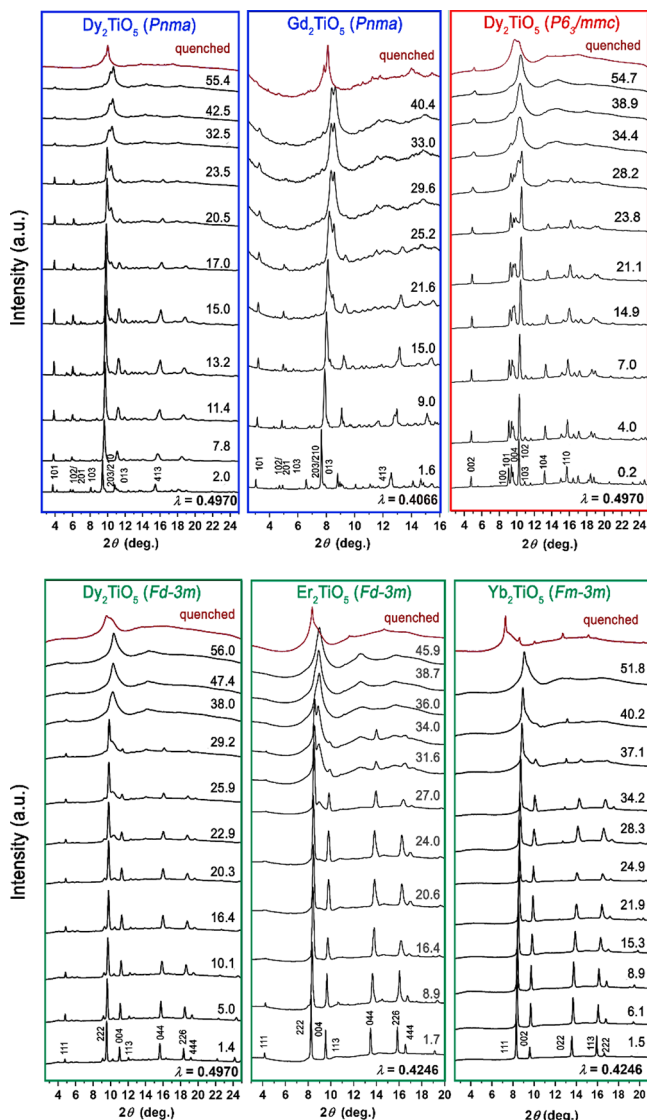


Figure 3. XRD patterns of $A_2\text{TiO}_5$ as a function of pressure at ambient temperature. All materials undergo sluggish reconstructive phase transformations. A high-pressure cotunnite-like phase is observed for all compositions. All patterns were collected *in situ* at high pressure. Values to the right of each pattern are the pressures in GPa. Wavelengths in Å are shown at the bottom of each panel.

the growth of broad bands caused by diffuse scattering at higher pressures.

High-Pressure Behavior of Orthorhombic $A_2\text{TiO}_5$. For *o*- Dy_2TiO_5 and *o*- Gd_2TiO_5 , the first phase transformation begins with a superlattice formation at pressures below 10 GPa. An enlarged figure of *o*- Dy_2TiO_5 and Gd_2TiO_5 at lower 2θ ranges, highlighting the diffraction maxima of the superlattice, is included **Figure 4a**. This first high-pressure phase in orthorhombic samples is consistent with that observed in isomorphous *o*- Nd_2TiO_5 and *o*- La_2TiO_5 , as reported by Zhang et al.,²² in which the superstructure phase was indexed as $P2_1am$.²² The refined XRD pattern of *o*- Gd_2TiO_5 in the present study, indexed with $P2_1am$, is shown in **Figure 4b**. According to Zhang et al., this new superstructure has Ti coordinated to nine oxygens, leading to a complete corner-shared TiO_5 polyhedral framework. The local bonding of this superstructure remains close to that of the precursor unit cell, except that the A-site cations are rearranged on the $a-b$ plane and the c axis increases

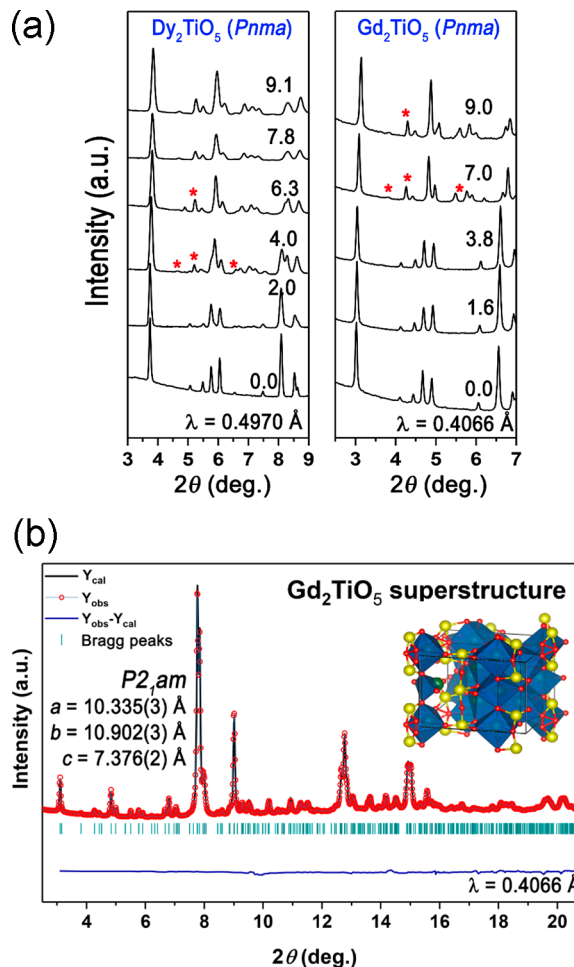


Figure 4. (a) XRD patterns of *o*- Dy_2TiO_5 and *o*- Gd_2TiO_5 up to ~9 GPa, highlighting the $Pnma$ to $P2_1am$ phase transformations. New peaks from $P2_1am$ are highlighted with red asterisks. Values to the right of each pattern are pressures in GPa. (b) Refinement of an XRD pattern collected from Gd_2TiO_5 pressurized to 7.0 GPa in a DAC. The simulated pattern (black line) fits well with the experimental data (red open circles). Bragg peak positions, represented by blue tick marks, confirm a well-indexed $P2_1am$ phase of Gd_2TiO_5 at 7.0 GPa. Deviations between the simulated and experimental data are minimal (blue line). The schematic diagram shows the structure simulated from the refined data. The same result was found in Dy_2TiO_5 at ~6.3 GPa.

to accommodate the corner-shared geometry.²² The indexed unit cell parameters are $a = 10.335$ Å, $b = 10.902$ Å, and $c = 7.376$ Å.

Above ~13 GPa, a second high-pressure phase becomes dominant in both *o*- Dy_2TiO_5 and *o*- Gd_2TiO_5 . This second high-pressure phase is evidenced by an increase in the scattering intensity of the (004) peak, lying between the (201/230) and (031) diffraction maxima. The intensity of the (004) peak is greater than that of the (201/230) diffraction maxima at pressures above 33 and 44 GPa for *o*- Dy_2TiO_5 and *o*- Gd_2TiO_5 , respectively, indicating changes to the morphology. Refinement of the unit cell parameters revealed an anisotropic volume reduction, in which the c axis of the unit cell decreases at a faster rate than do the a and b axes with increasing pressure. Reconstructive disordering is suspected to be responsible for the changes in XRD intensity and can be explained by the increase in the crystal face area along the a and

b axes, while the corner-shared TiO_5 polyhedra transition to edge-sharing along the *c* axis.

It is worth noting that the second high-pressure phase in *o*- Dy_2TiO_5 and *o*- Gd_2TiO_5 is different from that previously observed in isomorphous *o*- Nd_2TiO_5 and *o*- La_2TiO_5 by Zhang et al.²² In the study of Zhang et al., a hexagonal phase ($P6_3/mmc$) was identified at pressures above ~ 8 and 12 GPa for *o*- La_2TiO_5 and *o*- Nd_2TiO_5 , respectively.²² The different phase transformation in this study compared with that of Zhang et al. can be attributed to the difference in the A-site cation size. While the average long-range periodicity in all three samples appears to be the same, the larger A-site cations of Nd ($r_A = 0.98 \text{ \AA}$) and La ($r_A = 1.03 \text{ \AA}$) mean that these lanthanide elements are more “stuffed” into the matrix, leading to increased local atomic distances to accommodate the larger A-site cations. This “stuffing” leads to an increased ordering, which changes the phase transformation energetics and stability at high pressures. A very recent computational study reported that, as La replaces Dy, the A_1-O and A_2-O bond lengths increase by 1.16% and 1.19%, respectively.³⁹ The contrasting local structure of the *o*- La_2TiO_5 in comparison with *o*- Dy_2TiO_5 and *o*- Gd_2TiO_5 under ambient conditions as analyzed by X-ray PDF is shown in Figure S1 in the Supporting Information. As observed in Figure S1a, the A–O bond of *o*- La_2TiO_5 appears at a distance at least $\sim 0.3 \text{ \AA}$ farther away from those of *o*- Dy_2TiO_5 and *o*- Gd_2TiO_5 , owing to the increased A-site cation size. Indeed, the local ordering of the *o*- La_2TiO_5 is very similar to that of the *h*- Dy_2TiO_5 (in comparison with the local ordering in the orthorhombic structure) under ambient conditions. This similarity in the short-range order of La_2TiO_5 and Nd_2TiO_5 to a hexagonal phase at ambient pressure may explain the decreased activation energy barrier to the reconstructive transformation into a closely related hexagonal symmetry at higher pressures.

High-Pressure Behavior of Cubic A_2TiO_5 . As with the two-stage phase transformations in *o*- Dy_2TiO_5 and *o*- Gd_2TiO_5 , cubic A_2TiO_5 exhibits two major polymorphic changes as a function of pressure. The onset for the first high-pressure transformation in cubic A_2TiO_5 appears to resemble the second high-pressure phase of *o*- Dy_2TiO_5 and *o*- Gd_2TiO_5 : the growth of a new peak between the (222) and (004) diffraction maxima of the pyrochlore $Fd\bar{3}m$ structure (equivalent to (111) and (002) of the $Fm\bar{3}m$ structure). This new high-pressure phase appears at ~ 21 GPa for *p*- Dy_2TiO_5 , *p*- Er_2TiO_5 , and *df*- Yb_2TiO_5 . Unlike the case for the orthorhombic phase, however, the intensity of this new peak does not outweigh the strongest diffraction maxima of the cubic phases. This is attributed to the stronger diffraction maxima of pyrochlore or defect-fluorite peaks and/or the possible higher stability of the cubic A_2TiO_5 phases at a high-pressure range for which this phase is accessible.

A similar XRD pattern has previously been attributed to a defect-cotunnite-like phase and has been reported as a high-pressure polymorph of closely related $\text{A}_2\text{B}_2\text{O}_7$ -type ternary oxide compounds, as well as for single-cation AO_2 fluorite-structured oxides.^{40–44} Even when the contents of the rare-earth cation are increased relative to the $\text{A}_2\text{B}_2\text{O}_7$ composition, such that it partially occupies the B-site, leading to vacancies in the oxygen sublattice, the aliovalent solid solutions of A_2TiO_5 exhibit a similar phase evolution at high pressures. This high-pressure phase is common and typical of lanthanide-bearing, fluorite-derivative ternary complex oxides and actinide-bearing fluorite-structured oxides.^{44–46} Large strains, disorder, and random redistribution of cations and anions into solid solutions

under pressure contribute to the broadening of the XRD peaks. This broadening, combined with the presence of an amorphous domain, makes it a challenge to conclusively refine the XRD. First-principles calculations provide a more convincing argument by suggesting that the cotunnite phase has a lower enthalpy in comparison to the defect-fluorite or the compositionally equivalent amorphous phase, making it a more energetically favorable candidate at high pressure.^{47,48}

A second high-pressure polymorph is evidenced by the appearance of two new peaks: between the (113) and (044) and between the (044) and (226) diffraction maxima for *p*- Dy_2TiO_5 and *p*- Er_2TiO_5 at ~ 26 and 32 GPa, respectively, and between the (002) and (022) and between the (022) and (113) diffraction maxima for *df*- Yb_2TiO_5 at 28 GPa. For all samples, the appearance of these new peaks is quickly followed by the disappearance of the (044) diffraction maximum (or (022) in *df*- Yb_2TiO_5) above 36 GPa. At higher pressures, the patterns display large strain effects and some degree of amorphization, hindering refinement of the XRD patterns. Because *p*- Er_2TiO_5 retained most of its sharp peaks at the highest pressure reached, refinement was only attempted with *p*- Er_2TiO_5 . The positions of the diffraction maxima agree well with those of a cubic X-type phase ($Im\bar{3}m$), with unit cell parameter $a = 4.115(3) \text{ \AA}$. The phase is isostructural with the high-temperature phase in Ln_2O_3 sesquioxides.⁴⁹ Details of the phase are discussed in Recovered Phases.

High-Pressure Behavior of Hexagonal A_2TiO_5 . The high-pressure phase transformation in *h*- Dy_2TiO_5 begins with the disappearance of the (103) peak at 21 GPa. Concurrent with this peak disappearance is the growth of a new peak between the (004) and (102) diffraction maxima at a pressure of ~ 24 GPa. This peak seems to be exempt from strain effects and overlapping of the existing peaks and does not appear sharply until ~ 28 GPa. At pressures above ~ 36 GPa, this high-pressure phase becomes similar to the orthorhombic phase, suggesting that it could also be a defect-cotunnite-like phase. As with the orthorhombic phase, the superlattice (002) peak in hexagonal Dy_2TiO_5 remains even at the highest pressure reached (~ 55 GPa), which indicates a sluggish pressure-induced phase transformation from the hexagonal phase. The kinetically inhibited phase transformation requires very high pressures to overcome the larger energy barrier and causes a complete conversion into a metastable cotunnite-like phase.

Bulk Moduli of A_2TiO_5 . The pressures at which the phase transformations begin (P_{onset}) and complete ($P_{\text{completion}}$) are given in Table 2, which summarizes the experimental results. Note that, for materials going through two-stage phase transformations, only P_{onset} values of the disordered cotunnite-like phase are reported. In this study, there is no strong correlation between the onset of the high-pressure phase transition and the sample density. However, between the two *p*- A_2TiO_5 , for which the same pressure medium and experimental conditions were applied, the onset of the phase transition point is higher in *p*- Dy_2TiO_5 in comparison with *p*- Er_2TiO_5 . The increased propensity to transform into a cotunnite phase in pyrochlore materials with higher r_A value (Dy 0.91 vs Er 0.89 \AA) is in agreement with previous literature.⁵⁰ The differing stability ranges of the pyrochlore phases with different r_A/r_B values have been attributed to differences in their disordering energy. Substitution of a larger A-site cation increases the formation energy of anion Frenkel pairs and cation antisite defects, both of which are necessary for the phase transformation to occur, leading to an increased pressure transition

Table 2. Chemical Composition, A-Site Cationic Radius (r_A) under Ambient Conditions (Å), Space Group before Pressurization, Onset of High-Pressure Phase Transformation to a Cotunnite-Like Phase (P_{onset} in GPa), Transformation Completion Pressure ($P_{\text{completion}}$ in GPa), Bulk Modulus (B_0 in GPa), and Calculated Density (g/cm³) under Ambient Conditions^a

compound	r_A	space group	P_{onset}	$P_{\text{completion}}$	B_0	density
Dy ₂ TiO ₅	0.91	<i>Pnma</i>	13.2	32.5	175.9(7)	6.95
Gd ₂ TiO ₅	0.93	<i>Pnma</i>	15.0	29.6	236.0(4)	6.62
Dy ₂ TiO ₅	0.91	<i>Fd\bar{3}m</i>	22.9	33.7	221.5(10)	7.30
Er ₂ TiO ₅	0.89	<i>Fd\bar{3}m</i>	20.6	36	228.6(13)	7.39
Yb ₂ TiO ₅	0.85	<i>Fm\bar{3}m</i>	21.9	37	367.2(9)	7.96
Dy ₂ TiO ₅	0.91	<i>P6₃/mmc</i>	21.1	34	218.5(6)	6.32

^aFor B_0 , the values in parentheses refer to the 1σ uncertainty in the last given digit. For *o*-Dy₂TiO₅ and *o*-Gd₂TiO₅, P_{onset} values noted here are for when a cotunnite-like phase is seen.

point. While this observation was only reported for $A_2Ti_2O_7$ - and $A_2Zr_2O_7$ -type pyrochlore compounds, this study demonstrates that the trend is consistent for A_2TiO_5 materials of related structures.

The pressure dependence of the unit cell volume on pressure for all samples are plotted in Figure 5. All data are fitted using a

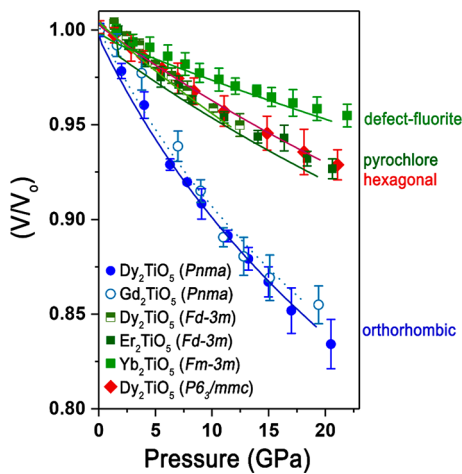


Figure 5. Pressure–volume relationships for A_2TiO_5 materials. Volumes are derived from Rietveld refinement of high-pressure XRD data. Error bars are obtained from the positional variation in the diffraction maxima. All data were fit to the second-order Birch–Murnaghan equation of state. Compressibility curves indicate that *o*- A_2TiO_5 phases (*Pnma*) are noticeably more compressible than the cubic A_2TiO_5 and *h*- A_2TiO_5 (*P6₃/mmc*).

second-order Birch–Murnaghan equation of state only up to ~ 15 – 20 GPa to avoid the effects of structural distortions⁵¹ and nonhydrostaticity of the pressure media.²⁵ The calculated bulk moduli are given in Table 2. A systematic comparison of the bulk moduli indicates that *o*- A_2TiO_5 (*Pnma*) phases are the most compressible, while *df*-Yb₂TiO₅ is the least compressible. The volume changes of *p*- and *h*- A_2TiO_5 are very similar and lie between those of *o*- and *df*- A_2TiO_5 .

4. Recovered Phases. XRD patterns of the pristine (black lower lines) and quenched (red upper lines) samples are shown in Figure 6. The only sample that partially recovers its initial structure upon pressure release is *df*-Yb₂TiO₅ (*Fm\bar{3}m*).

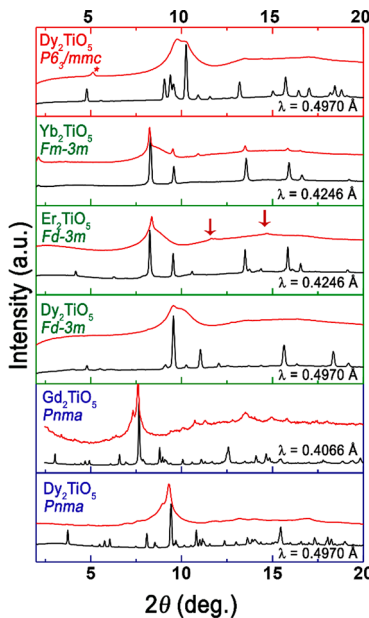


Figure 6. XRD patterns of precompression ambient pressure (black lines) and postcompression quenched (red lines) phases of all samples studied. All patterns were normalized to the same maximum intensity. Red arrows for the *p*-Er₂TiO₅ panel indicate the two new peaks characteristic of the X-type *Im3m* phase.

Although the amorphous domains are retained upon quenching, diffraction maxima representative of the defect-fluorite structure reappear under ambient conditions. For all other samples, the broad peaks of the high-pressure phase remain, indicating that the phase transformation is reconstructive and irreversible and that some fraction of the high-pressure phase is recoverable to ambient conditions.

In *o*- A_2TiO_5 , the quenched phase contains a fraction of the high-pressure disordered cotunnite-type phase. Although amorphous domains are present, the positions of the diffraction maxima are consistent with those of the high-pressure cotunnite phase. Similar results are observed upon pressure release for *h*-Dy₂TiO₅. However, in the case of *h*-Dy₂TiO₅, the incomplete transformation of the (002) peak remains (red asterisk in Figure 6), once again highlighting the kinetic constraints in *h*-Dy₂TiO₅.

An interesting quenched phase appears in cubic A_2TiO_5 , where the X-type high-pressure phase is stabilized to ambient conditions. In addition to the XRD refinement, ex situ analysis of the quenched sample using bright-field TEM was performed (Figure 7). As seen in the fast Fourier transformation (FFT) images next to Figure 7a, the quenched phase of *p*-Er₂TiO₅ exhibits a mixture of crystalline and amorphous domains. Both X-ray (Figure 6) and electron (Figure 7b) diffraction from the recovered sample agree well with the *Im\bar{3}m* phase, further confirming the stabilization of the metastable X-type phase. The formation of this X-type phase is most likely possible due to the cationic radius ratio of this composition. With a decreased r_A value of cubic Er₂TiO₅, relative to the other compositions studied, the high-pressure cotunnite phase is energetically unfavorable, and the high bond strength and structural rigidity of the compound prevent full amorphization. The material then slowly transforms into a nonequilibrium X-type phase and retains this structure upon pressure release. The stabilization of this phase under ambient conditions is particularly interesting due to its characteristic high ionic

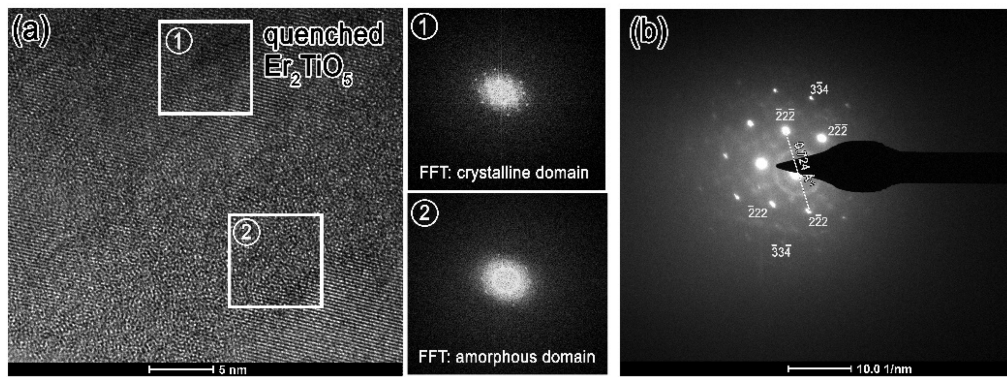


Figure 7. (a) Bright-field TEM image of p- Er_2TiO_5 quenched from ~ 50 GPa. Insets 1 and 2 show both the crystalline and amorphous domains of quenched p- Er_2TiO_5 . (b) Electron diffraction image of quenched p- Er_2TiO_5 .

conductivity, caused by the low occupancy of its anion sublattice resulting in high oxygen diffusion.^{52,53} This phase was first observed as a nonrecoverable high-temperature polymorph of Ln_2O_3 .⁴⁹ Later, Lang et al. reported the same structure in $\text{Gd}_2\text{Zr}_2\text{O}_7$ subjected to simultaneous irradiation with swift heavy ions at a pressure of ~ 40 GPa.⁵⁴ Tracy et al. produced the same structure from irradiation of Ln_2O_3 ($\text{Ln} = \text{Tm}, \text{Lu}$) sesquioxides with ions of comparable energy.⁵² This X-type phase exhibits a body-centered-cubic cation sublattice, with lanthanides in the 2a position, along with a highly disordered, low-occupancy anion sublattice rich in constitutional vacancies.⁵² To the author's knowledge, this is the first reported observation of a pressure-induced X-type phase in complex oxides of the $\text{A}_2\text{O}_3-\text{BO}_2$ series. Thus, alongside swift heavy ion irradiation and the combined effects of ion irradiation and pressure, this study shows that pressure alone can form this unique structure when the optimal composition and precursor structure are selected.

CONCLUSIONS

The structural evolution of A_2TiO_5 compounds at high pressures was investigated. All samples underwent reconstructive phase transformations, and a summary of the high-pressure phase transformation pathways is illustrated in Figure 8. The stages of the phase transformation process and the onset pressure of high-pressure phase formation are different for different samples, depending on the initial structures. However,

all samples reach a defect cotunnite-like phase at a certain range of pressure. The high-pressure phase transformation to the disordered cotunnite-like phase of A_2TiO_5 is in agreement with the previously reported high-pressure phase of structurally and compositionally related $\text{A}_2\text{B}_2\text{O}_7$ compounds, for which $\text{B} = \text{Ti}, \text{Zr}, \text{Hf}$.^{42-44,47,50,51} We demonstrate, for the first time, the formation of a pressure-induced X-type phase in p- Er_2TiO_5 , which can be partially recovered to ambient conditions. This X-type phase exhibits both anion sublattice disordering and cation sublattice disordering. The combination of such disordering implies high oxygen mobility and thermomechanical stability, making the material a desirable candidate as an electrolyte in solid oxide fuel cells. Overall, the potential implications resulting from fundamental scientific insights produced in this work are 2-fold: they provide an improved understanding of A_2TiO_5 structure-type performance in extreme environments, enabling material design to better withstand these environments, and they illustrate a possible means of synthesizing new, functional materials with unique properties.

ASSOCIATED CONTENT

Supporting Information

The Supporting Information is available free of charge on the ACS Publications website at DOI: [10.1021/acs.inorgchem.7b03106](https://doi.org/10.1021/acs.inorgchem.7b03106).

X-ray PDF analysis and X-ray diffraction patterns of orthorhombic A_2TiO_5 ($\text{A} = \text{La}, \text{Gd}, \text{Dy}$). ([PDF](#))

AUTHOR INFORMATION

Corresponding Author

*E-mail for S.P.: sulgije@stanford.edu.

ORCID

Sulgije Park: [0000-0001-5875-4727](https://orcid.org/0000-0001-5875-4727)

Karena W. Chapman: [0000-0002-8725-5633](https://orcid.org/0000-0002-8725-5633)

Changyong Park: [0000-0002-3363-5788](https://orcid.org/0000-0002-3363-5788)

Jacob Shamblin: [0000-0002-1799-5353](https://orcid.org/0000-0002-1799-5353)

Notes

The authors declare no competing financial interest.

ACKNOWLEDGMENTS

This work was supported by the Energy Frontier Research Center *Materials Science of Actinides* funded by the U.S. Department of Energy (DOE), Office of Science, Office of Basic Energy Sciences (Grant No. DE-SC0001089). Part of this work was performed at HPCAT (Sector 16), Advanced Photon

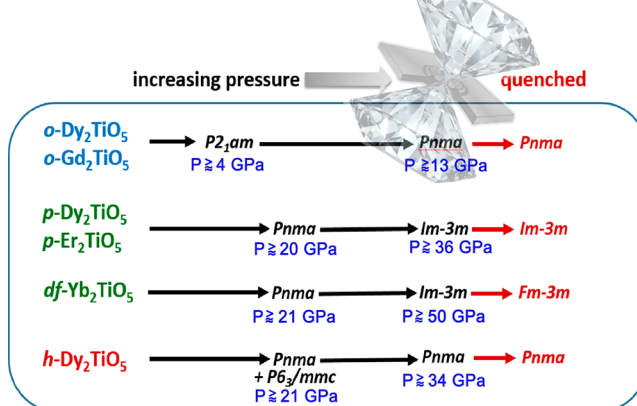


Figure 8. Summary of the high-pressure phase transformations in A_2TiO_5 .

Source (APS), Argonne National Laboratory. C.P. acknowledges the support of the DOE-BES/DMSE under Award No. DE-FG02-99ER45775. HPCAT operations are supported by DOE-NNSA under Award No. DE-NA0001974, with partial instrumentation funding by NSF. The Advanced Photon Source is a U.S. Department of Energy (DOE) Office of Science User Facility operated for the DOE Office of Science by Argonne National Laboratory under Contract No. DE-AC02-06CH11357. Use of the Advanced Photon Source was supported by the Carnegie/Department of Energy Alliance Center (CDAC, DE-FC03-03NA00144). X-ray total scattering data were collected at the X-ray Science Division beamline 11 ID-B of the APS, ANL. S.P. acknowledges Olaf J. Borkiewicz and Kevin A. Beyer for their help in collecting high-energy X-ray diffraction and pair distribution function data.

■ REFERENCES

- (1) Pan, T. M.; Lin, J. C.; Wu, M. H.; Lai, C. S. Structural properties and sensing performance of high-k Nd_2TiO_5 thin layer-based electrolyte-insulator-semiconductor for pH detection and urea biosensing. *Biosens. Bioelectron.* **2009**, *24*, 2864–2870.
- (2) Augterson, R. D.; et al. Ion-irradiation resistance of the orthorhombic Ln_2TiO_5 ($\text{Ln} = \text{La}, \text{Pr}, \text{Nd}, \text{Sm}, \text{Eu}, \text{Gd}, \text{Tb}$ and Dy) series. *J. Nucl. Mater.* **2015**, *467*, 683–691.
- (3) Tracy, C. L.; et al. Structural response of A_2TiO_5 ($\text{A} = \text{La}, \text{Nd}, \text{Sm}, \text{Gd}$) to swift heavy ion irradiation. *Acta Mater.* **2012**, *60*, 4477–4486.
- (4) Zhang, J.; et al. Ion-irradiation-induced structural transitions in orthorhombic Ln_2TiO_5 . *Acta Mater.* **2013**, *61*, 4191–4199.
- (5) Sinha, A.; Sharma, B. P. Development of dysprosium titanate based ceramics. *J. Am. Ceram. Soc.* **2005**, *88*, 1064–1066.
- (6) Kim, H. S.; Joung, C. Y.; Lee, B. H.; Kim, S. H.; Sohn, D. S. Characteristics of $\text{Gd}_x\text{M}_y\text{O}_z$ ($\text{M} = \text{Ti}, \text{Zr}$ or Al) as a burnable absorber. *J. Nucl. Mater.* **2008**, *372*, 340–349.
- (7) Kramer, S. A.; Tuller, H. L. A novel titanate-based oxygen ion conductor: $\text{Gd}_2\text{Ti}_2\text{O}_7$. *Solid State Ionics* **1995**, *82*, 15–23.
- (8) Feighery, A. J.; Irvine, T. S.; Zheng, C. High Oxide Ion Conductivity in Non-Stoichiometric Pyrochlores and Fluorites in the Ternary System $\text{ZrO}_2\text{-Gd}_2\text{O}_3\text{-TiO}_2$. *Ionics* **1997**, *3*, 30–35.
- (9) Aldebert, P.; Dianoux, A. Neutron scattering evidence for fast ionic oxygen diffusion in the high temperature phases of La_2O_3 . *J. Phys.* **1979**, *40*, 1005–1012.
- (10) Jiang, Y.; Smith, J. R.; Robert Odette, G. Prediction of structural, electronic and elastic properties of $\text{Y}_2\text{Ti}_2\text{O}_7$ and Y_2TiO_5 . *Acta Mater.* **2010**, *58*, 1536–1543.
- (11) Petrova, M. a.; Grebenschikov, R. G. Specific features of the phase formation in the titanate systems $\text{Ln}_2\text{TiO}_5\text{-Ln}'_2\text{TiO}_5$ ($\text{Ln} = \text{La}, \text{Gd}, \text{Tb}, \text{Er}; \text{Ln}' = \text{Tb}, \text{Lu}$). *Glass Phys. Chem.* **2008**, *34*, 603–607.
- (12) Shepelev, Y. F.; Petrova, M. a. Crystal structures of Ln_2TiO_5 ($\text{Ln} = \text{Gd}, \text{Dy}$) polymorphs. *Inorg. Mater.* **2008**, *44*, 1354–1361.
- (13) Shepelev, Y. F.; Petrova, M. a.; Novikova, A. S. Crystal structure of the hexagonal modification of lutetium-stabilized gadolinium titanate $\text{Gd}_{1.5}\text{Lu}_{0.2}\text{TiO}_5$. *Glass Phys. Chem.* **2004**, *30*, 342–344.
- (14) Subramanian, M. a.; Aravamudan, G.; Subba Rao, G. V. Oxide pyrochlores — A review. *Prog. Solid State Chem.* **1983**, *15*, 55–143.
- (15) Chakoumakos, B. C. Systematics of the pyrochlore structure type, ideal $\text{A}_2\text{B}_2\text{X}_6\text{Y}$. *J. Solid State Chem.* **1984**, *53*, 120–129.
- (16) Shlyakhtina, A. V.; Belov, D. A.; Karyagina, O. K.; Shcherbakova, L. G. Ordering processes in Ln_2TiO_5 ($\text{Ln} = \text{Dy} - \text{Lu}$): The role of thermal history. *J. Alloys Compd.* **2009**, *479*, 6–10.
- (17) Lau, G. C.; McQueen, T. M.; Huang, Q.; Zandbergen, H. W.; Cava, R. J. Long- and short-range order in stuffed titanate pyrochlores. *J. Solid State Chem.* **2008**, *181*, 45–50.
- (18) Lau, G. C.; et al. Structural disorder and properties of the stuffed pyrochlore Ho_2TiO_5 . *Phys. Rev. B - Condens. Matter Mater. Phys.* **2007**, *76*, 1–7.
- (19) Shlyakhtina, A. V.; Savvin, S. N.; Levchenko, A. V.; Boguslavskii, M. V.; Shcherbakova, L. G. Heavily doped oxygen-ion conducting $\text{Ln}_{2+x}\text{Ti}_{2-x}\text{O}_7$ ($\text{Ln} = \text{Ho-Lu}; x = 0.44–0.81$) pyrochlores: Crystal structure, microstructure and electrical conductivity. *Solid State Ionics* **2008**, *179*, 985–990.
- (20) Garcia-Martinez, G.; Martinez-Gonzalez, L. G.; Escalante-Garcia, J.; Fuentes, A. F. Phase evolution induced by mechanical milling in $\text{Ln}_2\text{O}_3\text{-TiO}_2$ mixtures ($\text{Ln} = \text{Gd}$ and Dy). *Powder Technol.* **2005**, *152*, 72–78.
- (21) Huang, J. Microstructural Evolution of $\text{Dy}_2\text{O}_3\text{-TiO}_2$ powder mixtures during Ball Milling and Post-Milled Annealing. *Materials (Basel)* **2017**, *10*, 19.
- (22) Zhang, F. X.; Wang, J. W.; Lang, M.; Zhang, J. M.; Ewing, R. C. Pressure-induced structural transformations in lanthanide titanates: La_2TiO_5 and Nd_2TiO_5 . *J. Solid State Chem.* **2010**, *183*, 2636–2643.
- (23) Hammersley, A. P.; Svensson, S. O.; Hanfland, M.; Fitch, A. N.; Hausermann, D. Two-dimensional detector software: From real detector to idealised image or two-theta scan. *High Pressure Res.* **1996**, *14*, 235–248.
- (24) Qiu, X.; Thompson, J. W.; Billinge, S. J. L. PDFgetX2: a GUI-Driven Program to Obtain the Pair Distribution Function from X-Ray Powder Diffraction Data. *J. Appl. Crystallogr.* **2004**, *37*, 678.
- (25) Klotz, S.; Chervin, J.-C.; Munsch, P.; Le Marchand, G. Hydrostatic limits of 11 pressure transmitting media. *J. Phys. D: Appl. Phys.* **2009**, *42*, 075413.
- (26) Mao, H. K.; Xu, J.; Bell, P. M. Calibration of the ruby pressure gauge to 800 kbar under quasi-hydrostatic conditions. *J. Geophys. Res.* **1986**, *91*, 4673–4676.
- (27) Prescher, C.; Prakapenka, V. B. DIOPTAS: a program for reduction of two-dimensional X-ray diffraction data and data exploration. *High Pressure Res.* **2015**, *35*, 223.
- (28) Rodriguez-Carvajal, J. *Fullprof suite*; LLB Saclay and LCSIM Rennes, France, 2003.
- (29) Roisnel, T.; Rodríguez-Carvajal, J. WinPLOTR: A Windows Tool for Powder Diffraction Pattern Analysis. *Mater. Sci. Forum* **2001**, *378–381*, 118–123.
- (30) Angel, R. J.; Gonzales-Platas, J.; Alvaro, M. EosFit7c and a Fortran module (library) for equation of state calculations. *Z. Kristallogr. - Cryst. Mater.* **2014**, *229*, 405–419.
- (31) Gonzalez-Platas, J.; Alvaro, M.; Nestola, F.; Angel, R. J. EosFit7-GUI: a new graphical user interface for equation of state calculations, analyses and teaching computer programs EosFit7-GUI: a new graphical user interface for equation of state calculations, analyses and. *J. Appl. Crystallogr.* **2016**, *49*, 1377–1382.
- (32) Ahmad, J. F.; Alkammash, I. Y. Theoretical study of some thermodynamical properties for solid under high pressure using finite-strain EOS. *J. Assoc. Arab Univ. Basic Appl. Sci.* **2012**, *12*, 17–22.
- (33) Gaurav, S.; Sharma, B. S.; S, S. B.; Upadhyaya, S. Analysis of finite-strain equations of state for solids under high pressures. *Phys. B Condens. Matter* **2004**, *352*, 134–146.
- (34) Whittle, K. R.; et al. Ion-beam irradiation of lanthanum compounds in the systems $\text{La}_2\text{O}_3\text{Al}_2\text{O}_5$ and $\text{La}_2\text{O}_3\text{TiO}_2$. *J. Solid State Chem.* **2010**, *183*, 2416–2420.
- (35) Augterson, R. D.; et al. Crystal chemistry of the orthorhombic Ln_2TiO_5 compounds with $\text{Ln} = \text{La}, \text{Pr}, \text{Nd}, \text{Sm}, \text{Gd}, \text{Tb}$ and Dy . *J. Solid State Chem.* **2015**, *227*, 60–67.
- (36) Seymour, K. C.; Ribeiro, D.; McCormack, S. J.; Kriven, W. M. Relationship Between the Orthorhombic and Hexagonal Phases in Dy_2TiO_5 . *J. Am. Ceram. Soc.* **2016**, *99*, 3739–311744.
- (37) Zhang, J.; et al. Nanoscale phase transitions under extreme conditions within an ion track. *J. Mater. Res.* **2010**, *25*, 1344–1351.
- (38) Jiang, C.; Stanek, C. R.; Sickafus, K. E.; Uberuaga, B. P. First-principles prediction of disordering tendencies in pyrochlore oxides. *Phys. Rev. B: Condens. Matter Mater. Phys.* **2009**, *79*, 104203.
- (39) Liu, X.; et al. Insights into the radiation behavior of Ln_2TiO_5 ($\text{Ln} = \text{La-Y}$) from defect energetics. *Comput. Mater. Sci.* **2017**, *139*, 295–300.
- (40) Duclos, S. J.; Vohra, Y. K.; Ruoff, A. L. High-pressure x-ray diffraction study of CeO_2 to 70 GPa and pressure-induced phase

- transformation from the fluorite structure. *Phys. Rev. B: Condens. Matter Mater. Phys.* **1988**, *38*, 7755–7758.
- (41) Idiri, M.; Le Bihan, T.; Heathman, S.; Rebizant, J. Behavior of actinide dioxides under pressure. *Phys. Rev. B: Condens. Matter Mater. Phys.* **2004**, *70*, 014113.
- (42) Rittman, D. R.; et al. Strain engineered pyrochlore at high pressure. *Sci. Rep.* **2017**, *7*, 2236.
- (43) Turner, K. M.; et al. Pressure-induced structural modifications of rare-earth hafnate pyrochlore. *J. Phys.: Condens. Matter* **2017**, *29*, 255401.
- (44) Rittman, D. R.; et al. High-pressure behavior of $A_2B_2O_7$ pyrochlore ($A = Eu, Dy$; $B = Ti, Zr$). *J. Appl. Phys.* **2017**, *121*, 045902.
- (45) Idiri, M.; Le Bihan, T.; Heathman, S.; Rebizant, J. Behavior of actinide dioxides under pressure: UO_2 and ThO_2 . *Phys. Rev. B: Condens. Matter Mater. Phys.* **2004**, *70*, 014113.
- (46) Zhang, F. X.; Lang, M.; Becker, U.; Ewing, R. C.; Lian, J. High pressure phase transitions and compressibilities of $Er_2Zr_2O_7$ and $Ho_2Zr_2O_7$. *Appl. Phys. Lett.* **2008**, *92*, 011909.
- (47) Xiao, H. Y.; et al. Zirconate pyrochlores under high pressure. *Phys. Chem. Chem. Phys.* **2010**, *12*, 12472–12477.
- (48) Xiao, H. Y.; Gao, F.; Weber, W. J. Ab initio investigation of phase stability of $Y_2Ti_2O_7$ and $Y_2Zr_2O_7$ under high pressure. *Phys. Rev. B* **2009**, *80*, 212102–4.
- (49) Adachi, G.; Imanaka, N. The Binary Rare Earth Oxides. *Chem. Rev.* **1998**, *98*, 1479–1514.
- (50) Zhang, F. X.; et al. Phase stability and pressure dependence of defect formation in $Gd_2Ti_2O_7$ and $Gd_2Zr_2O_7$ pyrochlores. *Phys. Rev. Lett.* **2008**, *100*, 045503.
- (51) Zhang, F. X.; et al. Structural distortions and phase transformations in $Sm_2Zr_2O_7$ pyrochlore at high pressures. *Chem. Phys. Lett.* **2007**, *441*, 216–220.
- (52) Tracy, C. L.; Lang, M.; Zhang, F.; Trautmann, C.; Ewing, R. C. Phase transformations in Ln_2O_3 materials irradiated with swift heavy ions. *Phys. Rev. B: Condens. Matter Mater. Phys.* **2015**, *92*, 174101.
- (53) Aldebert, P.; Traverse, J. P. Etude Par Diffraction Neutronique des Structures de Haute Température de La_2O_3 et Nd_2O_3 . *Mater. Res. Bull.* **1979**, *14*, 303–323.
- (54) Lang, M.; et al. Nanoscale manipulation of the properties of solids at high pressure with relativistic heavy ions. *Nat. Mater.* **2009**, *8*, 793–797.